ANL-80-26

ANL-80-26

A LAGRANGIAN THREE-DIMENSIONAL FINITE-ELEMENT FORMULATION FOR THE NONLINEAR FLUID-STRUCTURAL RESPONSE OF REACTOR COMPONENTS

by

R. F. Kulak and C. Fiala

BASE TECHNOLOGY

ARGONNE NATIONAL LABORATORY, ARGONNE, ILLINOIS

Prepared for the U. S. DEPARTMENT OF ENERGY
under Contract W-31-109-Eng-38

DISCLAIMER

The facilities of Argonne National Laboratory are owned by the United States Government. Under the terms of a contract (W-31-109-Eng-38) among the U. S. Department of Energy, Argonne Universities Association and The University of Chicago, the University employs the staff and operates the Laboratory in accordance with policies and programs formulated, approved and reviewed by the Association.

MEMBERS OF ARGONNE UNIVERSITIES ASSOCIATION

The University of Arizona
Carnegie-Mellon University
Case Western Reserve University
The University of Chicago
University of Cincinnati
Illinois Institute of Technology
University of Illinois
Indiana University
The University of Iowa
Iowa State University
The University of Kansas
Kansas State University
Loyola University of Chicago
Marquette University
The University of Michigan
Michigan State University
University of Minnesota
University of Missouri
Northwestern University
University of Notre Dame
The Ohio State University
Ohio University
The Pennsylvania State University
Purdue University
Saint Louis University
Southern Illinois University
The University of Texas at Austin
Washington University
Wayne State University
The University of Wisconsin-Madison

Printed in the United States of America
Available from
National Technical Information Service
U. S. Department of Commerce
5285 Port Royal Road
Springfield, VA 22161

NTIS price codes
Printed copy: A03
Microfiche copy: A01

Distribution Category:
LMFBR--Safety (UC-79p)

ANL-80-26

ARGONNE NATIONAL LABORATORY
9700 South Cass Avenue
Argonne, Illinois 60439

A LAGRANGIAN THREE-DIMENSIONAL FINITE-ELEMENT FORMULATION FOR THE NONLINEAR FLUID-STRUCTURAL RESPONSE OF REACTOR COMPONENTS

by

R. F. Kulak and C. Fiala

Reactor Analysis and Safety Division

March 1980

THIS PAGE

WAS INTENTIONALLY

LEFT BLANK

TABLE OF CONTENTS

LIST OF FIGURES

LIST OF FIGURES

LIST OF TABLES

THIS PAGE

WAS INTENTIONALLY

LEFT BLANK

A LAGRANGIAN THREE-DIMENSIONAL FINITE-ELEMENT FORMULATION FOR THE NONLINEAR FLUID-STRUCTURAL RESPONSE OF REACTOR COMPONENTS

by

R. F. Kulak and C. Fiala

ABSTRACT

This report presents the formulations used in the NEPTUNE code. Specifically, it describes the finite-element formulation of a three-dimensional hexahedral element for simulating the behavior of either fluid or solid continua. Since the newly developed hexahedral element and the original triangular plate element are finite elements, they are compatible in the sense that they can be combined arbitrarily to simulate complex reactor components in three-dimensional space. Because rate-type constitutive relations are used in conjunction with a velocity-strain tensor, the formulation is applicable to large deformation problems. This development can be used to simulate (1) the fluid adjacent to reactor components and (2) the concrete fill found in large reactor head closures.

An algorithm is presented for integrating the elasto-plastic constitutive equations. It uses a subincrementation procedure and a yield-surface return scheme so that the end-of-step stress state lies on the yield surface.

The new element formulation was verified by comparison with problems having closed-form analytical solutions. The dynamic response of a concrete-filled deck structure which is one of the major components of a large Pool-type Liquid Metal Fast Breeder Reactor was investigated for a hypothetical core-disruptive accident. Also, the hydrodynamic element was used to simulate the fluid in a study of the fluid-structural interaction of a Pool Reactor In-tank Component.

I. INTRODUCTION

The safety evaluation of reactor components often involves the analysis of various types of structural/fluid elements: beams, plates, three-dimensional solid continua, three-dimensional fluids, etc. The explicit version of SADCAT[1] contained a flat, triangular plate element that was used for the analysis of hexcans and simple models of head closures.

Presented here is the development of a hexahedral finite element that can be used to simulate either a fluid or a solid in three-dimensional space. Thus, this element can be viewed as being both a hydrodynamic element and a solid element. This element can interact with the original SADCAT triangular-plate element to solve coupled fluid-structure interaction problems with a unified treatment. Also, this element can be used to simulate the pre-cracked structural effects of concrete.

With the current goal of developing a 1200-MWe reactor, it is necessary to assess the structural integrity of several of its main components. One of these components is the deck structure. Two recent studies[2,3] reviewed basic design concepts of large LMFBR's. These studies indicated that for both the pool- and loop-type deck structure, concrete would be one of the components of the deck. Generally, the deck itself is a composite of beams, plates, and concrete. Consequently, to model the concrete as a structural element, one must use a three-dimensional solid continuum element.

Other components that may be susceptible to structural damage during a hypothetical core-disruptive accident (HCDA) are the in-tank components suspended from the deck of a pool-type reactor. In particular, these components are the primary pumps and intermediate heat exchangers. Because these components are immersed in the large sodium pool, a meaningful structural analysis must include the interaction between the structural components and its surrounding fluid. Here it is necessary to simulate the fluid media with a hydrodynamic element. Also, note that both the deck structure and the in-tank component must be analyzed in three dimensions.

A three-dimensional hexahedral finite element was formulated so that it could represent either a hydrodynamic element or solid continuum element. Since both the hydrodynamic and solid elements are finite elements, they can be combined arbitrarily with the original plate finite element to represent complex, three-dimensional reactor structures.

A nonlinear elastoplastic constitutive algorithm was developed for use with the solid and plate elements. This algorithm is applicable for metals whose behavior can be treated by an isotropic hardening theory. A subincrementation procedure is used in conjunction with a yield-surface return scheme to ensure that the consistency condition is satisfied. The number of subincrements needed per time step is automatically determined based upon the inner product between the beginning-of-step normal to the yield surface and an estimated end-of-step normal. The algorithm can treat problems in which the material undergoes plastic behavior during the first time increment. In addition, reversed loading problems can be handled.

The above formulations are incorporated in a computer program and given the name NEPTUNE, which is based upon the quasi-acronym obtained from Nonlinear Elastic Plastic Three-dimensional Fluid Structure Interaction Code. It is the first three-dimensional fluid-structure interaction code developed at ANL.

II. THREE-DIMENSIONAL FINITE-ELEMENT FORMULATION

A. Governing Equations

We will here derive the finite-element equations for a single element based upon the principle of conservation of mechanical energy. The resulting form can be used to represent either a Lagrangian hydrodynamic or solid continuum element. The principle of conservation of mechanical energy for an element is given in integral form as

$$\frac{d}{dt}\int_V \tfrac{1}{2}\rho v_i v_i \, dV + \int_V \sigma_{ij}\dot{\epsilon}_{ij} \, dV - \int_S T_i v_i \, dS - \int_V \rho F_i v_i \, dV = 0, \tag{1}$$

where

ρ = density,

v_i, T_i, F_i = components of velocity, surface traction, and body force (per unit mass), respectively,

and

σ_{ij}, $\dot{\epsilon}_{ij}$ = components of Cauchy stress and velocity-strain tensors, respectively.

The velocity-strain tensor (rate-of-deformation tensor) is defined by

$$\dot{\epsilon}_{ij} = \tfrac{1}{2}(v_{i,j} + v_{j,i}), \tag{2}$$

where the comma denotes a spatial derivative. Note that $\dot{\epsilon}_{ij}$ is not a strain rate. The first two terms of Eq. 1 represent the time rate of change of the kinetic and internal energies of the element, respectively; the last two terms are the rates of work done on the element. Equation 1 is valid for any type of material, and there is no restriction on the size of the deformation gradients. Both the stress and velocity-strain tensors can be divided into hydrostatic and deviatoric components

$$\sigma_{ij} = S_{ij} - \rho\delta_{ij} \tag{3}$$

and

$$\dot{\epsilon}_{ij} = \dot{e}_{ij} + (1/3)\dot{\epsilon}_{kk}\delta_{ij}, \tag{4}$$

where

S_{ij}, $\dot{e}_{ij}$ = deviatoric components of the stress and velocity-strain tensors, respectively,

and

p, $\dot{\epsilon}_{kk}$ = hydrostatic pressure and cubical dilatation, respectively.

Using the above relations in Eq. 1, we have

$$\frac{d}{dt}\int_V \tfrac{1}{2}\rho v_i v_i \, dV - \int_V p\dot{\epsilon}_{kk} \, dV + \int_V S_{ij}\dot{\epsilon}_{ij} \, dV - \int_S T_i v_i \, dS - \int_V \rho F_i v_i \, dV = 0. \tag{5}$$

The second integral on the left-hand side of Eq. 5 represents a contribution due to the hydrostatic behavior of the material, and the third integral represents a contribution due to the deviatoric behavior of the material. Thus, for an inviscid fluid, the third integral is not calculated, but for a solid continuum, both integrals must be evaluated.

In the finite-element method, the velocity field for each element is approximated by

$$v_i = \varphi_I \dot{d}_{iI}, \tag{6}$$

where v_i is the velocity in the ith direction, φ_I is the shape function for the Ith node, and $\dot{d}_{iI}$ is the velocity of the Ith node in the ith direction. Using the above approximation for the velocity in the conservation of mechanical energy expression Eq. 5, we have

$$\frac{d}{dt}\int_V \tfrac{1}{2}\rho \dot{d}_{kI}\varphi_I\varphi_J\dot{d}_{kJ} \, dV - \int_V p\varphi_{I,k}\dot{d}_{kI} \, dV + \int_V S_{ij}G_{Iijk}\dot{d}_{kI} \, dV$$

$$- \int_S T_k\varphi_I\dot{d}_{kI} \, dS - \int_V \rho F_k\varphi_I\dot{d}_{kI} \, dV = 0 \tag{7}$$

where

$$G_{Iijk} = \tfrac{1}{2}(\varphi_{I,j}\delta_{ik} + \varphi_{I,i}\delta_{jk}) - \tfrac{1}{3}\varphi_{I,k}\delta_{ij} \tag{8}$$

and δ_{ij} is the Kronecker delta.

Taking the indicated time derivatives, we obtain for a single finite element

$$\dot{d}_{kI}\left(m_{IJ}\ddot{d}_{kJ} + f_{kI}^{int,h} + f_{kI}^{int,d} - f_{kI}^{T} - f_{kI}^{b}\right) = 0, \tag{9}$$

where the element's consistent mass is given by

$$m_{IJ} = \int_V \rho\varphi_I\varphi_J \, dV, \tag{10}$$

the hydrostatic internal nodal-force matrix by

$$f_{kI}^{int,h} = -\int_V p\varphi_{I,k}\, dV, \tag{11}$$

the deviatoric internal nodal-force matrix by

$$f_{kI}^{int,d} = \int_V S_{ij} G_{Iijk}\, dV, \tag{12}$$

and the external nodal-load matrices by

$$f_{kI}^{T} = \int_S T_k \varphi_I\, dS, \tag{13}$$

and

$$f_{kI}^{b} = \int_V \rho F_k \varphi_I\, dV. \tag{14}$$

Since Eq. 9 must be valid for arbitrary motions, it must be true for arbitrary $\dot{d}_{kI}$; thus, the term in parentheses must vanish. The general equation of motion of a finite element is given by

$$m_{IJ}\ddot{d}_{kJ} + f_{kI}^{int,h} + f_{kI}^{int,d} - f_{kI}^{T} - f_{kI}^{b} = 0. \tag{15}$$

The formulation of this equation differs from the usual approach because the internal nodal forces are divided into hydrostatic and deviatoric parts. It should also be pointed out that Eq. 15 is identical to the form used in SADCAT. Thus, the above formulation is compatible with the earlier formulation and can be directly incorporated into the code. Equation 15 is the equation of motion of a single finite element; however, the global form of the equations of motion for the entire structure can be obtained by adding, in a consistent manner, the equations of motion for all the elements. Since this procedure is well known, it is not presented here.

B. Hydrodynamic Element

We will now develop the specific form of the internal nodal force matrix for a hydrodynamic element. The element is an eight-node hexahedron (see Figs. 1 and 2). This element has a node located at each of its eight corners. The element shape functions φ_i used here are the trilinear functions described by Zienkiewicz:[4]

$$\varphi_i = \tfrac{1}{8}(1 + \xi\xi_i)(1 + \eta\eta_i)(1 + \zeta\zeta_i) \tag{16}$$

where ξ, η, and ζ are the natural coordinates of the element (Fig. 2). For example, the shape function for node 1 is

$$\varphi_1 = \tfrac{1}{8}(1 + \xi)(1 + \eta)(1 - \zeta). \tag{17}$$

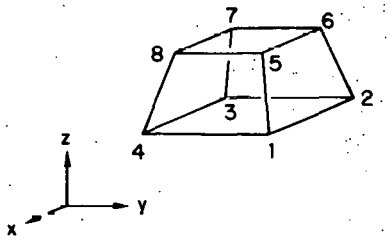

Fig. 1. Arbitrary Hexahedron in Global (x, y, z) Coordinate System

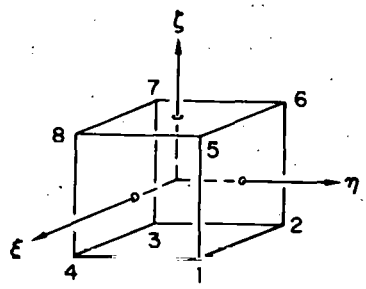

Fig. 2. Hexahedron after transformation into Local Natural (ξ, η, ζ) Coordinate System

We are primarily interested in problems in which the fluid can be treated as inviscid; thus, there are no shear stresses, which means that the deviatoric internal nodal forces are zero. Therefore, only the hydrostatic internal nodal forces need to be computed.

The method for computing the hydrostatic internal nodal forces proposed by Kennedy and Belytschko[5] will be followed. From Eqs. 9 and 11 the following relation for the rate of internal work for an element is given by

$$-\int_V p\dot{\epsilon}_{kk}\, dV = \dot{d}_{kI} f_{kI}^{int,h}. \tag{18}$$

Now we treat the pressure field within each element as a constant that reduces the integral in Eq. 18 to the form

$$\int_V p\dot{\epsilon}_{kk}\, dV = p\int_V \dot{\epsilon}_{kk}\, dV = p\dot{V}, \tag{19}$$

where $\dot{V}$ is the rate-of-volume change. This change can be expressed in linear form by

$$\dot{V} = H_{kI}\dot{d}_{kI}, \tag{20}$$

where H_{kI} depends only upon the nodal coordinates.

From Eqs. 18-20 we obtain the following expression for the hydrostatic internal nodal forces

$$f_{kI}^{int,h} = -pH_{kI}. \tag{21}$$

We obtain the form for these forces by determining H_{kI} from Eq. 20 as follows: First, the expression for the volume of a generic element is determined, and second, the temporal derivative of the volume gives the form for H_{kI}. Because of the difficulty in computing the volume of an element arbitrarily oriented in the global-coordinate system, we transform the element into its natural-coordinate system. Thus the volume, V, of the element is given by

$$V = \int_V dx\, dy\, dz = \int_\Omega \mathcal{J}\, d\xi\, d\eta\, d\zeta, \tag{22}$$

where $\mathcal{J}$ is the Jacobian of the transformation from the global (x, y, z) system to the natural (ξ, η, ζ) system. The final expression for the volume is obtained here by evaluating the right-most integral in Eq. 22 with a one-point integration scheme at the center of the hexahedron. The above procedure gives the following form for the hydrostatic internal nodal forces

$$f_{iI}^{int,h} = -\frac{p}{16}\Big[X_{jPJ}(X_{kKM} - X_{kNL}) - X_{jKM}(X_{kPJ} - X_{kNL}) + X_{jNL}(X_{kPJ} - X_{kKM})\Big], \tag{23}$$

where, for example, X_{jPJ} is defined to be

$$X_{jPJ} \equiv X_{jP} - X_{jJ}. \tag{24}$$

Here X_{jP} is the jth component of the coordinate of node P. The appropriate node numbers are given in the permutation table (Table I).

TABLE I. Permutation Table

I	J	K	L	M	N	P
1	2	3	4	5	6	8
2	3	4	1	6	7	5
3	4	1	2	7	8	6
4	1	2	3	8	5	7
5	8	7	6	1	4	2
6	5	8	7	2	1	3
7	6	5	8	3	2	4
8	7	6	5	4	3	1

Equation 10 defines the consistent mass matrix for the hydrodynamic element. It is a 24 x 24 nondiagonal matrix. When the consistent mass matrix is used in the equations of motion (Eq. 15), they become a set of coupled equations whose solution requires matrix inversion. To circumvent matrix inversions, we will use a diagonal mass matrix, which is formed by lumping the masses at the nodes. Now the equations of motion become uncoupled, and their solution is quite efficient. Note that the triangular plate element was also formulated with a diagonal mass matrix. In the explicit version of SADCAT, the equations of motion are integrated using an explicit central-difference temporal integrator. The numerical studies of Kreig and Key[6] showed that the combination of a diagonal mass matrix and the explicit central-difference time-integration method leads to accurate and economical solutions.

C. Continuum Element

The fluid element was formulated by considering only the hydrostatic (mean) components of stress and strain rates, which gave the formulation for the hydrostatic, internal nodal-force matrix. In this section we will develop the formulation for the deviatoric, internal nodal-force matrix that is obtained from the deviatoric components of the stress and strain rates. The combination of the hydrostatic and deviatoric internal forces provides the capability for modeling three-dimensional solid continua.

The deviatoric internal nodal force for an element was given (Eq. 12) by

$$f_{kI}^{int,d} = \int_V S_{ij} G_{Iijk} \, dV, \tag{25}$$

where the coefficient G_{Iijk} is a function of the element shape functions φ_m as defined in Eq. 8.

To determine the form for the deviatoric internal forces, we must evaluate the integral on the right-hand side of Eq. 12. Because a closed-form analytical expression is not tractable, we performed a numerical integration. Barlow[7] has indicated that there exist optimal points for calculating accurate stresses within a finite element. For the eight-node hexahedron used here, this optimal location is at the origin of the local natural-coordinate system (ξ, η, ζ). Therefore, the numerical integration required in Eq. 25 was performed using a one-point (optimal) integration scheme. Also, the integration was performed in the local natural-coordinate system because of numerical efficiencies. Therefore the deviatoric internal nodal forces are given by

$$f_{kI}^{int,d} = \int_V S_{ij} G_{Iijk} \, dV = \int_\Omega S_{ij} G_{Iijk} \rho \, d\Omega. \tag{26}$$

Evaluating the right-most integral in Eq. 26 gives the following expression for the components of the deviatoric internal nodal forces:

$$f_{iI}^{int} = \frac{1}{128\rho}\Big\{\Big[X_{jpJ}(X_{kKM} - X_{kNL}) + X_{jKM}(X_{kJL} - X_{kPN}) + X_{jLN}(X_{kJP} - X_{kKM})\Big]S_{ii} + \Big[X_{kPJ}(X_{iKM} - X_{iNL}) + X_{kKM}(X_{iJL} - X_{iPN}) + X_{kLN}(X_{iJP} - X_{iKM})\Big]S_{ij} + \Big[X_{iPJ}(X_{jKM} - X_{jNL}) + X_{iKM}(X_{jJL} - X_{jPN}) + X_{iLN}(X_{jJL} - X_{jKM})\Big]S_{ik}\Big\}. \quad (27)$$

The internal nodal forces for a solid continuum element are given by the sum of the hydrostatic and deviatoric nodal forces

$$f_{kI}^{int} = f_{kI}^{int,h} + f_{kI}^{int,d}. \quad (28)$$

A diagonal-mass matrix is also used for the solid continuum element.

D. Constitutive Relations

In this section we will describe the constitutive equations used to represent the material response of the following material types: fluid, concrete, and elastoplastic solid.

1. Fluid

The state of stress in a deforming fluid is given by

$$\sigma_{ij} = -p\delta_{ij} + f_{ij}(\dot{\epsilon}_{ij}), \quad (29)$$

where

p = thermodynamic pressure

f_{ij} = tensor-value function.

The thermodynamic pressure is determined by the kinetic equation of state, which is of the form

$$p = p(\rho, T), \quad (30)$$

where ρ is the density and T is the absolute temperature. For the class of problems we are interested in, we can consider the fluid to be isotropic. Furthermore, we are interested in problems in which the wave-propagation aspect dominates, so we can neglect the viscous behavior of the fluid. Thus, the stress state becomes isotropic and is given by

$$\sigma_{ij} = -p\delta_{ij}. \tag{31}$$

Now the equation of state (Eq. 30) for our frictionless fluid reduces to

$$p = p(\rho). \tag{32}$$

The explicit form used in the code is

$$p = K\frac{\Delta\rho}{\rho_0}, \tag{33}$$

where K is the bulk modulus of the fluid and the zero subscript refers to the original state.

From the equation of mass conservation for a Lagrangian element we have

$$\rho V = \rho_0 V_0. \tag{34}$$

In terms of the element volume, the pressure is given by

$$p = K\left(\frac{V_0}{V} - 1\right). \tag{35}$$

The above form of the equation of state for a fluid element is coded in the program. Other forms, when needed, can be readily incorporated.

2. Concrete

The material response of concrete is taken to be linear elastic. The reason for choosing this material model was the nature of the problem we are interested in solving. The problem is to determine the dynamic response of a pool-type deck structure. This structure is a composite of beams, plates, and concrete fill. The concrete fill is primarily a radiation shield. Its effect on the ultimate structural integrity of the deck is believed to be of second-order importance because of the likelihood of cracking under the extreme load conditions of a core-disruptive accident. However, since the structural effect of the concrete will affect the dynamic response of the deck, it should be included in the model. Also, although the above material model cannot treat the postcracking phenomenon, it can provide valuable information as to the locations of cracks and the time at which the onset of cracking occurs in the concrete fill.

The constitutive equation for concrete is of the form

$$\sigma^{\nabla}_{ij} = C_{ijkl}\dot{\epsilon}_{kl}, \tag{36}$$

in which the Jaumann stress rate σ^{∇}_{ij} is defined by

$$\sigma^{\nabla}_{ij} = \dot{\sigma}_{ij} - \sigma_{im}\dot{\omega}_{mj} - \sigma_{jn}\dot{\omega}_{ni}, \tag{37}$$

where the spin tensor $\dot{\omega}_{kl}$ is given by

$$\dot{\omega}_{kl} = \tfrac{1}{2}(v_{k,l} - v_{l,k}). \tag{38}$$

The stress rate can be separated into hydrostatic and deviatoric components given by

$$\sigma^{\nabla}_{ij} = \tfrac{1}{3}\dot{\sigma}_{kk}\delta_{ij} + S^{\nabla}_{ij}, \tag{39}$$

where

$$\dot{\sigma}_{kk} = -3\dot{p}. \tag{40}$$

In terms of these components, the constitutive relation becomes

$$\dot{\sigma}_{kk} = 3K\dot{\epsilon}_{kk} \tag{41}$$

and

$$S^{\nabla}_{ij} = 2G\dot{e}_{ij}, \tag{42}$$

where K and G are the bulk and shear moduli, respectively, for concrete.

Since the internal forces (Eq. 27) depend on the total stress values and the constitutive relations only provide the stress rates, we must obtain the total stresses at the current time from the stresses at the previous time step and the current stress increment. The stress increment is obtained from the stress rates by

$$\Delta\sigma_{kk} = \dot{\sigma}_{kk}\Delta t \tag{43}$$

and

$$\Delta S_{ij} = S^{\nabla}_{ij}\Delta t + \dot{\omega}_{ik}S_{kj}\Delta t - S_{ik}\dot{\omega}_{kj}\Delta t. \tag{44}$$

The total stresses at the current time step are given by

$$\sigma_{kk}(t + \Delta t) = \sigma_{kk}(t) + \Delta\sigma_{kk} \tag{45}$$

and

$$S_{ij}(t + \Delta t) = S_{ij}(t) + \Delta S_{ij}. \tag{46}$$

To determine the onset of cracking in the concrete fill, we must choose and utilize a simple criterion. A crack is said to initiate when a principal stress equals or exceeds a maximum tensile value σ_{mt}. Thus the onset of cracking occurs when

$$\sigma_{mt} = \max(\sigma_I, \sigma_{II}, \sigma_{III}), \tag{47}$$

where σ_I, σ_{II}, and σ_{III} are the eigenvalues of the stress tensor σ_{ij}.

The above treatment of concrete allows us to account for the structural effect of concrete and to identify the location and time at which cracking occurs. The treatment of postcracking behavior is not considered.

3. Elastoplastic Solid

The stress-strain-rate relations for an elastoplastic solid are presented below. The form used is limited to metal plasticity.

To begin, we must define several concepts and terms. Earlier we divided the velocity strain, stress, and Jaumann stress rate into dilatational and deviatoric parts (Eqs. 3, 4, and 39). Now we will further divide the deviatoric velocity strain into elastic and plastic parts, given by

$$\dot{e}_{ij} = \dot{e}^e_{ij} + \dot{e}^p_{ij}. \tag{48}$$

The dilatational stress is related to the velocity strain through Eq. 41 and the stress-rate deviator is related to the velocity-strain deviator by the hypoelastic relation

$$S^{\nabla}_{ij} = 2G\dot{e}^e_{ij} = 2G\left(\dot{e}_{ij} - \dot{e}^P_{ij}\right). \tag{49}$$

The plastic velocity strain is determined from a potential-flow law by

$$\dot{e}^p_{ij} = \dot{\lambda}\frac{\partial f}{\partial S_{ij}}, \tag{50}$$

where $\dot{\lambda}$ is a constant of proportionality and f is a yield function.

In our work we are using a von Mises yield function given by

$$f = S_{ij}S_{ij} - R^2(\bar{\epsilon}_p) = 0 \tag{51}$$

where R is the radius of a hypersphere in ninespace. It is related to a universal-response function by

$$R(\bar{\epsilon}_p) = \sqrt{\tfrac{2}{3}}\,\sigma_0(\bar{\epsilon}_p), \tag{52}$$

where σ_0 can be interpreted as the yield stress for a uniaxial specimen. The accumulated plastic strain is defined in terms of the plastic velocity strain as

$$\bar{\epsilon}_p = \int_0^t \dot{\bar{\epsilon}}^p \, dt, \tag{53}$$

where

$$\dot{\bar{\epsilon}}^p = \left(\tfrac{2}{3}\dot{e}^p_{ij}\dot{e}^p_{ij}\right)^{1/2}. \tag{54}$$

During plastic loading the stress must lie on the yield surface, which leads to the consistency condition given by

$$\dot{f} \equiv 0. \tag{55}$$

In terms of our yield function the consistency condition is given by

$$\dot{f} = S_{ij}S^{\nabla}_{ij} - R\dot{R} = 0. \tag{56}$$

Since our hardening function only depends on the accumulated plastic strain, its temporal derivative is given by

$$\dot{R} = \frac{dR}{d\bar{\epsilon}_p}\dot{\bar{\epsilon}}_p. \tag{57}$$

By using Eqs. 50, 51, and 54, we obtain the form

$$\dot{R} = \sqrt{\frac{2}{3}}\frac{dR}{d\bar{\epsilon}_p}R\dot{\lambda}. \tag{58}$$

By using Eqs. 49-51, 56, and 58, we solve for $\dot{\lambda}$, which is given by

$$\dot{\lambda} = \frac{S_{ij}\dot{e}_{ij}}{\left(1 + \frac{1}{G\sqrt{6}}\frac{dR}{d\bar{\epsilon}_p}\right)2R^2}. \tag{59}$$

With $\dot{\lambda}$ known we can determine the plastic strain rate (Eq. 50) and use it in Eq. 49 to find the stress rate.

E. Elastoplastic Constitutive Algorithm

The above equations are in differential form and must be integrated to yield total-stress values. The numerical method used for this integration is presented below. A prime objective of the algorithm is to integrate the differential equations so that the stress state satisfies the consistency condition (Eq. 56) exactly. Also, the algorithm must be able to determine the various loading-unloading processes.

During a time step a material may strain in any of the following regimes:

1. Loading
2. Unloading
3. Unloading-reloading.

The following plastic-loading relations determine the type of loading:

$$\left.\begin{array}{lll} \dfrac{\partial f}{\partial S_{ij}} S^{\nabla}_{ij} < 0 & \text{unloading,} & \\ \dfrac{\partial f}{\partial S_{ij}} S^{\nabla}_{ij} = 0 & \text{neutral loading,} & \\ \dfrac{\partial f}{\partial S_{ij}} S^{\nabla}_{ij} > 0 & \text{loading.} & \end{array}\right\} \tag{60}$$

The loading regime occurs when the beginning-of-step stress state is either inside the yield surface or on the yield surface and the end-of-step stress state lies on the yield surface. The unloading regime is when the beginning-of-step stress lies on the yield surface and the end-of-step stress is inside the yield surface. The unloading-reloading regime occurs when the strain increment is such that both the beginning-of-step stress and the end-of-step stress lie on the yield surface, but the loading path during the step traverses through the elastic region bounded by the yield surface.

To describe the algorithm used to obtain the stress increments, we define $S^{(1)}_{ij}$ as the beginning-of-step stress state (Fig. 3), S^{*}_{ij} as the estimated end-of-step stress state, and $S^{(2)}_{ij}$ as the end-of-step stress state. The algorithm first computes the end-of-step stress state based on the assumption that the loading process will be elastic; thus the first estimate of end-of-step stress is given by

$$S^{*}_{ij} = S^{(1)}_{ij} + \Delta S^{e}_{ij}, \tag{61}$$

where the elastic deviatoric-stress increment is obtained by evaluating Eq. 49 with the plastic strain rate equal to zero and then using Eq. 44. Now if both the initial stress state $S_{ij}^{(1)}$ and the end-of-step stress state S_{ij}^{*} are within the elastic region bounded by the yield surface then S_{ij}^{*} is the exact end-of-step stress $S_{ij}^{(2)}$ (see Fig. 3). On the other hand, if $S_{ij}^{(1)}$ is in the elastic region and S_{ij}^{*} is outside the yield surface, then the step must be divided into two parts: elastic and elastoplastic. The treatment of the elastic part is identical to the previous case. The plastic part is discussed in general below.

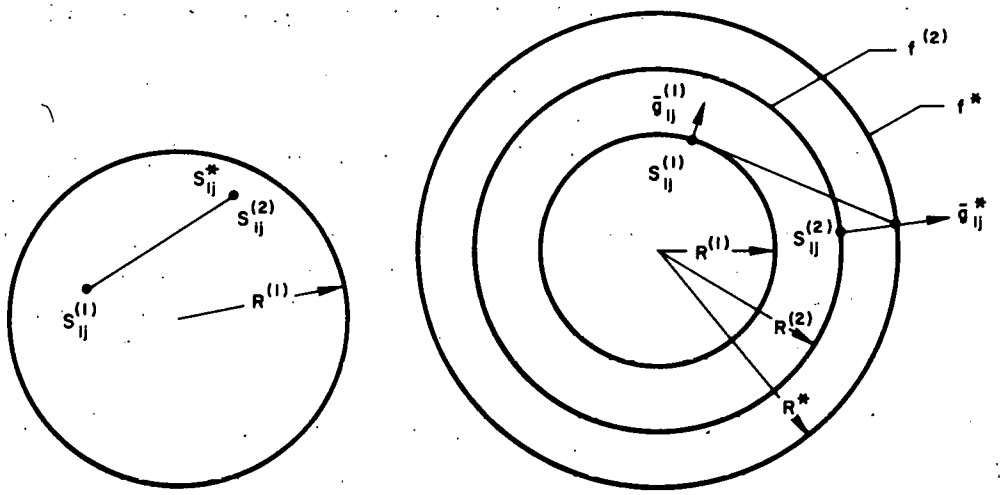

Fig. 3. Stress Space Showing Stress States, Yield Surfaces, and Normals Used in the Constitutive Algorithm. The yield surfaces are shown as circles for illustrative purposes and are in reality hyperspheres in ninespace.

We now describe the formulation used to obtain the end-of-step stress when plastic loading occurs. To begin, we assume that the stress state has been advanced to the yield surface and consider this stress to be the stress $S_{ij}^{(1)}$ in the following discussion. We note that the quantity $\partial f/\partial S_{ij}$ is the normal vector to the loading surface, say, g_{ij}. Therefore Eq. 50 can be restated as

$$\dot{e}_{ij}^{p} = \dot{\lambda} g_{ij}. \tag{62}$$

At the beginning of the step the normal $g_{ij}^{(1)}$ is known. Now we must determine the change in plastic-strain increment Δe_{ij}^{p} that occurs during the step. This increment is determined from

$$\Delta e_{ij}^{p} = \int_{t_1}^{t_2} \dot{e}_{ij}^{p}\, dt = \int_{t_1}^{t_2} g_{ij}(t)\dot{\lambda}\, dt. \tag{63}$$

The right-most integral above can be expressed in term of a sum as

$$\Delta e_{ij}^{p} = \lim_{N\to\infty} \sum_{n=1}^{N} g_{ij}^{(n)} \dot{\lambda}^{(n)} \Delta t^{(n)}. \tag{64}$$

When the value of N is equal to ∞, the sum equals the integral, and when N is finite, the sum approximates the integral. When N is equal to 1, we have a single-step procedure. In single-step procedures, the assumption is usually made that during the time step the strain increment is small enough that the normal does not change significantly; thus the strain increment is given by

$$\Delta e_{ij}^{p} = g_{ij}^{(1)} \dot{\lambda} \Delta t. \tag{65}$$

The estimate for the stress state S_{ij}^{*} and the associated normal g_{ij}^{*} at the end of the step can be calculated in the usual manner. The end-of-step normal can be compared to the beginning-of-step normal to determine if the above assumption is valid. If the two normals are equal or nearly so, then the computed stress is accurate. On the other hand, if the normals differ significantly, the plastic-strain increment should be calculated by

$$\Delta e_{ij}^{p} = \sum_{n=1}^{N} g_{ij}^{(n)} \dot{\lambda}^{(n)} \Delta t^{(n)}. \tag{66}$$

Now the problem becomes that of determining the number of subincrements N needed to compute Δe_{ij}^{p} accurately. To begin, let $S_{ij}^{(1)}$ and $S_{ij}^{(2)}$ be the stress states at the beginning and end of the step and let $g_{ij}^{(1)}$ and $g_{ij}^{(2)}$ be their respective normals to the yield surfaces $f^{(1)}$ and $f^{(2)}$ (see Fig. 3). Also, let us define a yield surface f^{*} generally not equal to $f^{(1)}$ or $f^{(2)}$.

The procedure proposed is as follows: First, compute an approximation of the stress state S_{ij}^{*} at the end of the step, based on the assumption that the normal vector to the yield surface does not change during the step. Then determine the components of the unit normal vector $\bar{g}_{ij}^{*}$, based on the approximated, end-of-step stress state S_{ij}^{*}, that is,

$$\bar{g}_{ij}^{*} = \frac{S_{ij}^{*}}{\|S_{ij}^{*}\|}, \tag{67}$$

where $\|S_{ij}^{*}\|$ is the Euclidean norm of S_{ij}^{*}. An estimate of the error occurring during the step is obtained by examining the inner product of the beginning-of-step normal $\bar{g}_{ij}^{(1)}$ and the end-of-step normal g_{ij}^{*}, which is expressed by

$$\bar{g}_{ij}^{(1)} \cdot \bar{g}_{ij}^{*} = \cos\theta. \tag{68}$$

The angle θ is used here as a measure of the error in the end-of-step stress state. A value of zero for theta indicates that the initial and final normals are collinear, and hence $\bar{g}_{ij}$ is constant during the step; thus for this case, end-of-step stress $S_{ij}^{(2)}$ is equal to S_{ij}^{*}. When the angle θ is greater than zero, the normal $\bar{g}_{ij}$ varies during the step and the subincrementing procedure should be used.

The above subincrementing method will increase the accuracy of the end-of-step stresses considerably when compared to a single-step method. However, because the end-of-step stress is based upon a linear predictor (Eq. 49), it does not satisfy the consistency condition stated in Eq. 56. Therefore, even though the subincrementing procedure has reduced the amount of drift from the yield surface it has not eliminated drifting.

In order to satisfy the consistency condition, a yield-surface return scheme was formulated. The yield-surface return formulation is described below. The object of this method is to return the stress S_{ij}^{*} from f^{*} to its image $S_{ij}^{(2)}$ on $f^{(2)}$. The unit normal vector to the estimated yield surface f^{*} is computed from Eq. 67 and is used to obtain a correlation stress defined by

$$\Delta S_{ij}^{c} = -\Delta S^{c} \bar{g}_{ij}^{*}, \tag{69}$$

where the scalar ΔS^{c} is the difference in radii between the estimated yield surface f^{*} and the yield surface $f^{(2)}$ determined from a universal response function evaluated at the equivalent plastic strain $\bar{\epsilon}_{p}^{*}$; that is,

$$\Delta S^{c} = R^{*} - R^{(2)}(\bar{\epsilon}_{p}^{*}) = (S_{ij}^{*} S_{ij}^{*})^{1/2} - \sqrt{\tfrac{2}{3}}\,\sigma_{0}(\bar{\epsilon}_{p}^{*}). \tag{70}$$

This yield-surface return method is applied at the end of each substep. This implies that the consistency condition is satisfied throughout the substep procedure.

The constitutive algorithm is used to evaluate the stress state when the material of the three-dimensional solid-continuum element is elastoplastic. It has also replaced the original algorithm used with the triangular plate element.

F. Artificial Viscous Stresses

The numerical solution of certain transient problems results in high-frequency oscillations that are not present in the analytical solution. These spurious oscillations are due to frequency cutoff of a discrete mesh and can be eliminated by viscosities. In this report we are using an explicit temporal integrator which has no artificial viscosities so spurious oscillations with a frequency equal to the highest mesh frequency are produced. Also, our discretized equations of motion do not contain any type of damping.

Therefore, to reduce or eliminate spurious oscillations when they occur, we will follow a common approach and introduce artificial viscous stresses, a form of numerical damping.

Belytschko et al.[8] presented the following form for a viscous stress to damp out the highest mode in a two-dimensional element:

$$\sigma_{ij}^{v} = d_L \rho \sqrt{A} [(C_1 - C_2)\dot{\epsilon}_{kk}\delta_{ij} + 2C_2\dot{\epsilon}_{ij}], \tag{71}$$

where C_1 and C_2 are the dilatational and shear-wave speeds, respectively, A the area of the element, ϵ_{ij} the strain, and d_L a fraction of critical damping for the highest mode. Here we will use a similar form for the three-dimensional hexahedral element. Since the stresses are separated into hydrostatic and deviatoric components, we will also separate the viscous stresses into these components. Specifically, the respective forms used for the hydrostatic and viscous stresses are given by

$$p^v = -\tfrac{1}{3}\sigma_{ii}^{v} = -d_L \rho h(C_1 - \tfrac{1}{3}C_2)\dot{\epsilon}_{ii}, \tag{72}$$

and

$$S_{ij}^{v} = 2d_L \rho h C_2 \dot{e}_{ij}, \tag{73}$$

where h is a characteristic length, and the remaining symbols retain their previous definitions.

The characteristic length here was taken to be the length of the smallest side of the hexahedron. The deviatoric viscous stress (Eq. 73) is linearly related to the velocity strain, which is an objective tensor. Therefore, the deviatoric viscous stress is also objective (i.e., frame-indifferent) and it can be used for large-deformation problems. Similarly, since the viscous pressure is a scalar quantity, it is also frame-indifferent and thus applicable to large-deformation problems.

The above viscous stresses are added to the total stresses as determined from the constitutive relations. Thus, for problems in which viscous stresses are used, the internal forces (Eqs. 11 and 12) are given by

$$f_{kI}^{int,h} = \int_v (p + p^v)\varphi_{I,k}\, dV, \tag{74}$$

and

$$f_{kI}^{int,d} = \int_v (S_{ij} + S_{ij}^{v})G_{Iijk}\, dV. \tag{75}$$

The above approach indicates that the inclusion of viscous stress, in effect, adds another set of internal forces to the equations of motion.

III. RESULTS

The above developments were implemented into the NEPTUNE code. In this section we present sample problems which illustrate the accuracy and applicability of these developments to simulate fluid-structure interactions in various three-dimensional configurations. The first group of problems compares NEPTUNE code results to analytical solutions or to other computer-code predictions. These problems are designed to check the performance of the new element against known results. The last two problems illustrate the applicability of the code to the structural dynamics of reactor components.

A. Dynamic Response of Two Concentric Tubes Separated by a Fluid

The first problem studied was that of two concentric tubes separated by a fluid (see Fig. 4). The inner tube was subjected to the pressure-time history shown in Fig. 5. The radial displacement of the inner cylinder (see Fig. 6) was computed by the STRAW and NEPTUNE codes. There is good agreement between the two codes, indicating that the newly added three-dimensional fluid element is operating properly.

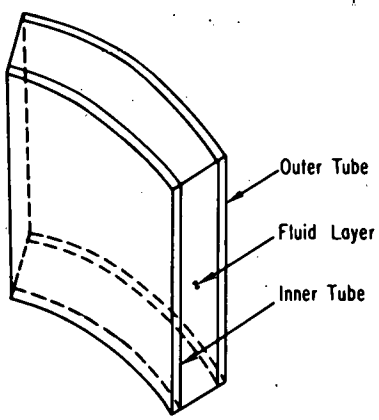

Fig. 4

Section of Two Concentric Tubes Separated by a Fluid Layer

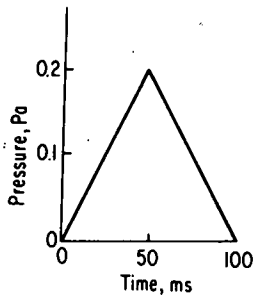

Fig. 5

Pressure–Time History Applied to Inside of Inner Tube

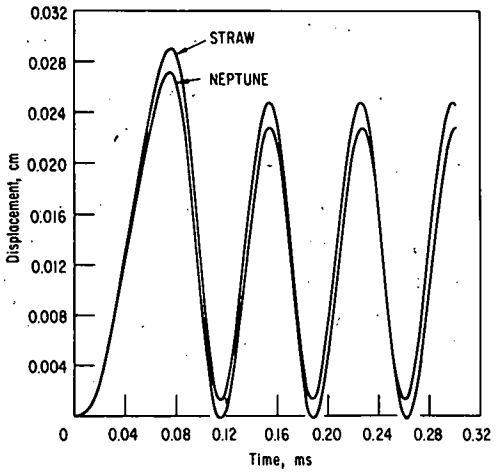

Fig. 6

Comparison between STRAW and NEPTUNE Predictions for Inner-tube Radial Displacement

B. Compression-wave Propagation down a Fluid Column

The second problem considered was that of a pressure wave traveling down a fluid column. The finite-element mesh for this problem is shown in Fig. 7. The NEPTUNE-predicted pressure history at location "A" is shown in Fig. 8. As seen from the results, there is a spurious oscillation in the code-predicted pressures. This oscillation is not found in the analytical solution. The finite-element solution predicts a pressure increase, which starts earlier than predicted by the analytical solution; the code solution overpredicts the pressure and oscillates about the analytical solution with decreasing amplitude. In order to snub these oscillations, artificial viscosity has been incorporated into the fluid elements. A second run was made in which the viscosity corresponded to the case of critical damping. The results are shown in Fig. 8. Except for a slight overshoot, the addition of artificial viscosity has eliminated the undesirable oscillations. This second run is in good agreement with the analytical solution.

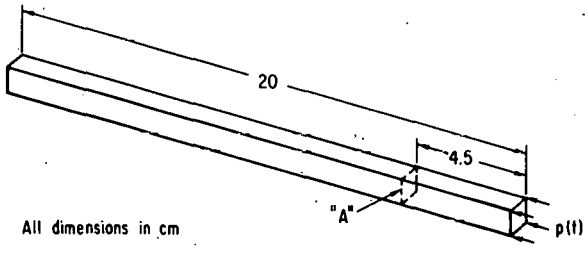

Fig. 7. Finite-element Mesh for Studying a Pressure Pulse Traveling down a Fluid Column

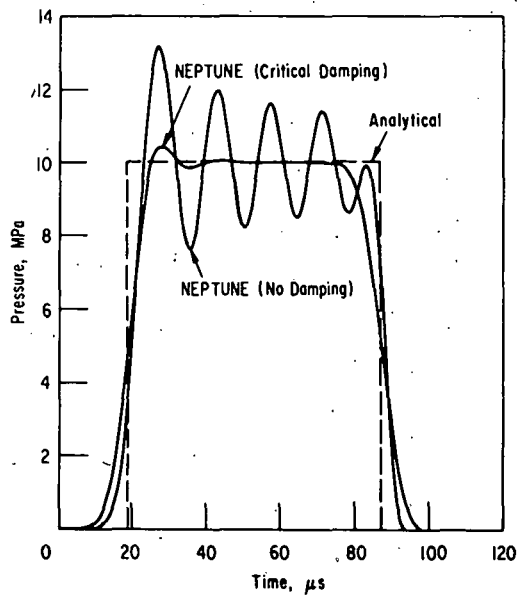

Fig. 8. Pressure-Time History at Location "A" in Fig. 7

C. Wave Propagation in a Fluid Emanating from a Cylindrical Cavity

The problem studied was a compression wave traveling through a fluid contained within an infinite cylinder (see Fig. 9) with an outer radius of 40 cm. A cylindrical cavity of 20-cm radius was located in the center of the fluid cylinder. At time zero, a step pressure was applied and maintained at the cavity-fluid interface. Analytically, this problem reduced to a one-dimensional wave-propagation problem in cylindrical coordinates. However, in three-dimensional Cartesian space the problem was two-dimensional; that is, motion occurred in the x and y directions. The finite-element model for

this problem is shown in Fig. 10. The model consisted of 20 fluid elements with a height h equal to 1 cm. The cavity radius was 20 cm, and the outer-fluid boundary radius was 40 cm. The fluid model was taken to be a 2.86° sector ($\Delta\theta = 2.86°$) of the physical cylinder (see Fig. 9). The measure used to evaluate the accuracy of the fluid-element response to the prescribed loading was the geometric pressure attenuation. From the analytical solution it was known that the fluid pressure attenuates inversely as the square root of the radial distance; that is,

$$\frac{P_2}{P_1} = \sqrt{\frac{r_1}{r_2}}, \tag{76}$$

where P_i is the fluid pressure at radius r_i. The computed responses for the fluid pressure were compared at several locations, with the analytical solution in Fig. 11. The code-computed pressures at various radial locations compared well with the analytical predictions.

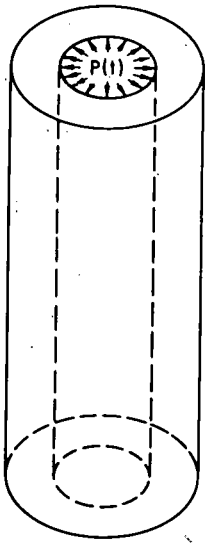

Fig. 9

Cylindrically Contained Fluid with an Internal Pressurized Cavity

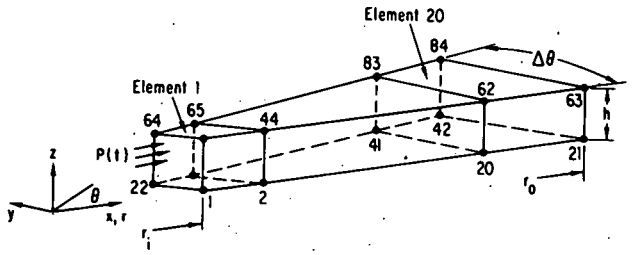

Fig. 10

Finite-element, Three-dimensional Fluid Model

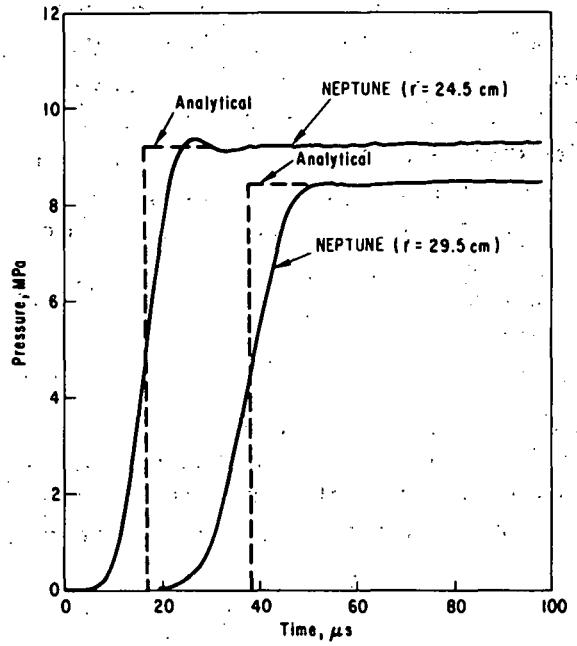

Fig. 11. Comparison between Analytical and NEPTUNE Results for Pressure Attenuations in a Cylindrical Configuration. Calculations were performed using artificial viscosity.

D. Wave Propagation in a Fluid Emanating from a Spherical Cavity

Our next comparative problem was similar to the previous problem, except that the compression wave was spherical. The physical problem considered was that of a compression wave emanating from a pressurized spherical cavity. The cavity radius r_i was 10 cm and the fluid radius r_o at the outer boundary was 20 cm (see Fig. 12). The finite-element model, shown in Fig. 13 contained 20 three-dimensional fluid elements. The elements were bounded by the angles $\Delta\varphi$ and $\Delta\theta$; both of these angles were equal to 9°. Note that even though this problem is reduced to a one-dimensional problem in spherical coordinates, it is a three-dimensional problem in Cartesian coordinates. All the nodes in the finite-element mesh underwent motion in the x, y, and z directions. The pressure-attenuation ability of an element was also used in this problem as an estimate of the accuracy for that element. For the spherical-wave problem, the pressure attenuates inversely as its radial distance; that is

$$\frac{P_2}{P_1} = \frac{r_1}{r_2}. \qquad (77)$$

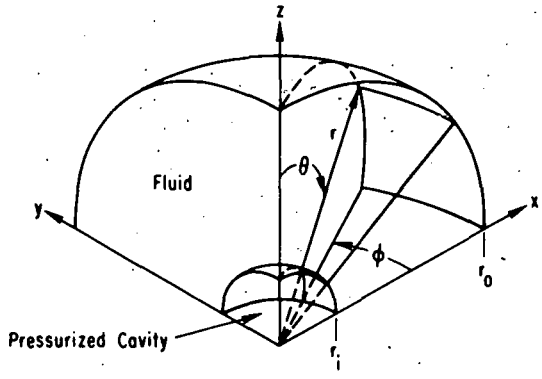

Fig. 12. A Pressurized Spherical Cavity in a Fluid Medium

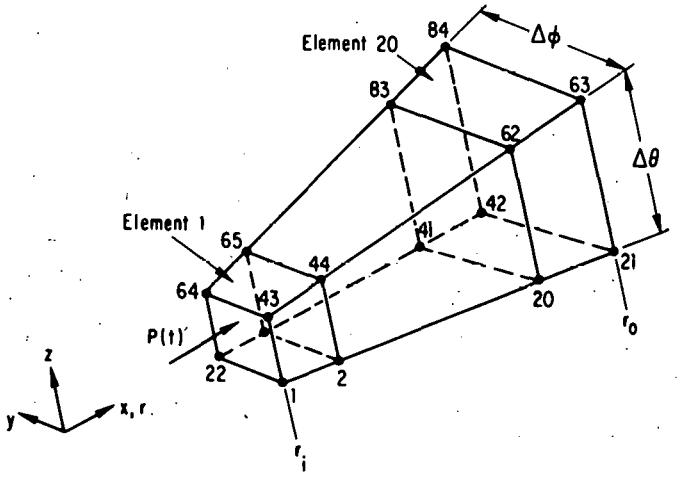

Fig. 13. Finite-element Model for Spherical-wave Study

A comparison between analytically predicted and NEPTUNE-predicted pressure attenuations at various radial locations (see Fig. 14) gave good agreement.

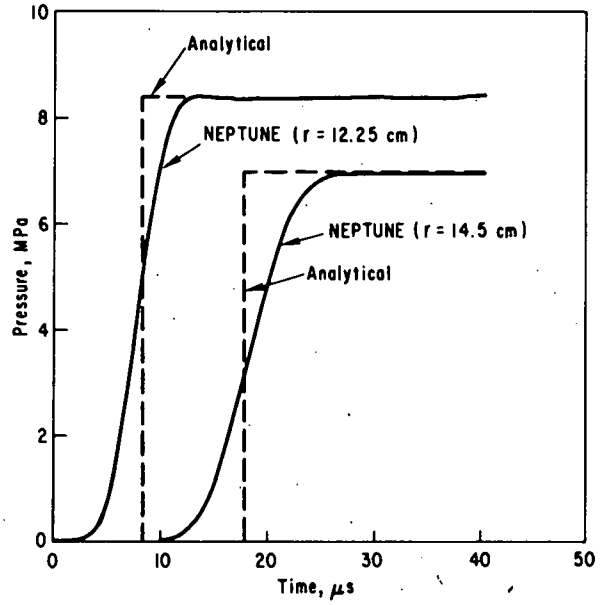

Fig. 14

Comparison between Analytical and NEPTUNE Results for Pressure Attenuations in a Spherical Configuration. Calculations were performed using artificial viscosity.

E. Fluid-Structural Interaction of Two Concentric Cylinders Separated by a Sodium Layer

The combined fluid-structural problem presented here is the dynamic response of two finite-length concentric cylinders (see Fig. 15) separated by a sodium layer and loaded by a pressure pulse acting over part of the inner cylinder. Both cylinders were 30.48 cm long and 1.016 mm thick; the nominal radius of the inner cylinder was 5.08 cm. A layer of sodium 2.54 mm thick separated the cylinders. A 100-μs triangular pulse (see Fig. 16) with a peak pressure of 20.7 MPa (at 50 μs) was applied to a central 15.24-cm-long region around the inner circumference of the inner cylinder. Because of symmetry in both loading and geometry, the NEPTUNE finite-element model (see Fig. 17) for this problem consisted of a 10° sector 15.24 cm high. Twenty-four triangular plate elements were used to model the cylinders (12 for the inner and 12 for the outer) and six fluid-hexahedral elements for the sodium layer. The material properties are given in Table II.

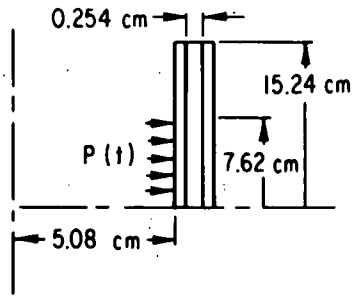

Fig. 15. Concentric Cylinders Separated by a Sodium Layer

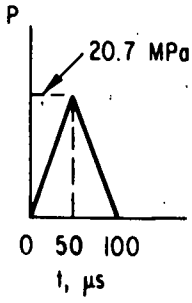

Fig. 16. Applied Pressure Pulse

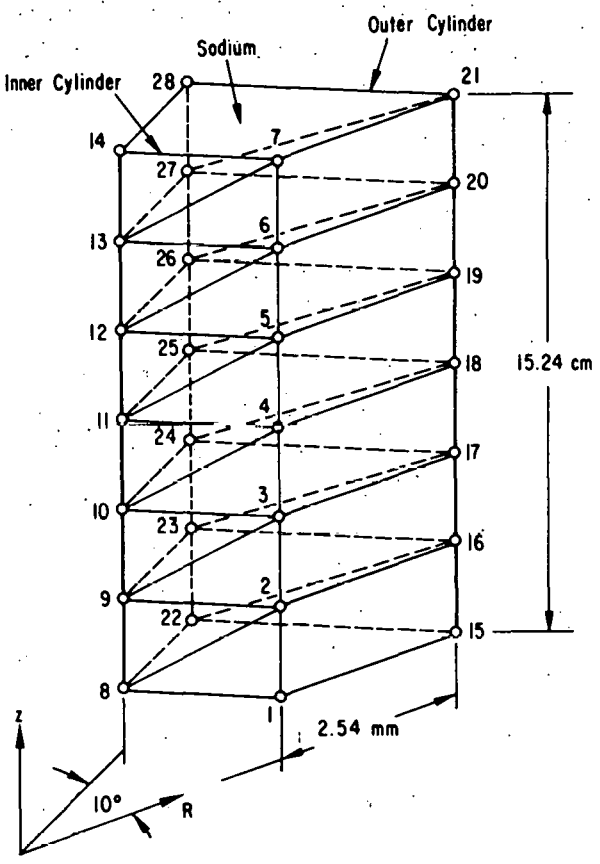

Fig. 17

Finite-element Model for Concentric Cylinders

TABLE II. Material Properties for Sample Problem E

	Cylinders (steel at elevated temperature)	Fluid (sodium)
Density (g/cm^3)	7.8	0.826
Young's modulus (GPa)	152	-
Bulk modulus (GPa)	-	4.05
Yield stress (MPa)	517	-
Tangent modulus (MPa)	414	-

The NEPTUNE-predicted response was compared with the predicted response of WHAM.[9] The radial-displacement history of the inner cylinder at the line of symmetry is shown in Fig. 18. The NEPTUNE and the WHAM results compare reasonably well in displacement amplitude, response frequency, and amplitude variation. However, the NEPTUNE results indicate a slightly stiffer behavior.

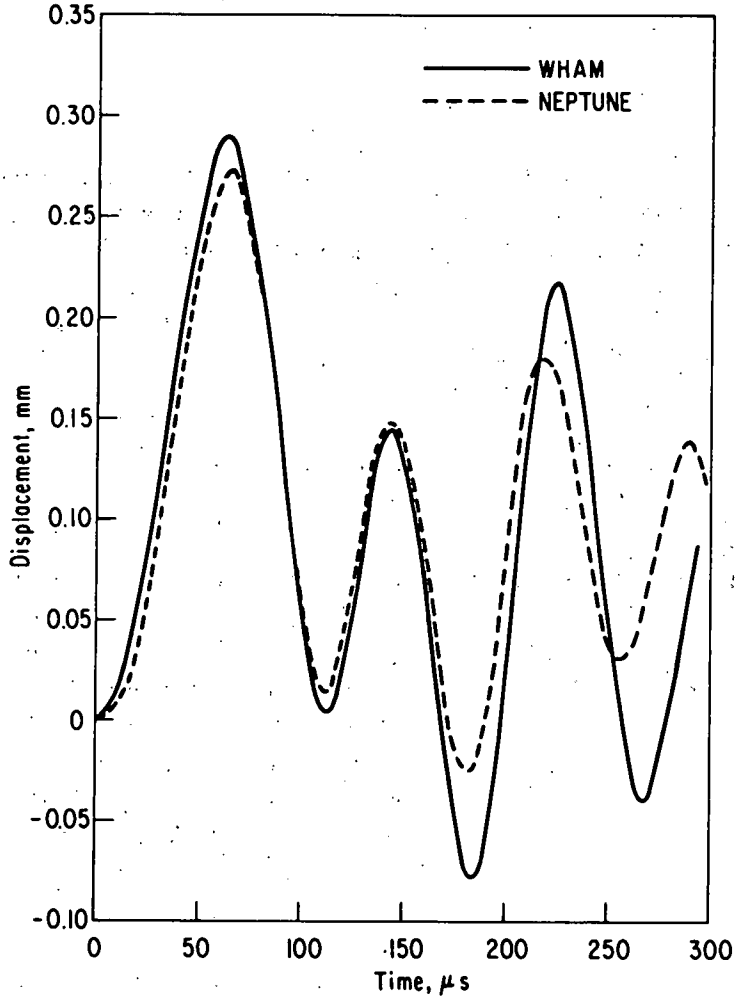

Fig. 18. Comparison between NEPTUNE and WHAM Results for Radial Displacement of Inner Cylinder at Line of Symmetry

F. S-wave Propagation in an Elastic, Infinite Plate

The problem studied was the propagation of a plane shear wave in an infinite, elastic plate. The plate was taken to be 50 cm thick in the Z direction and infinite in the X and Y directions. The front face of the plate was subjected to the shear loading given by

$$\sigma_{ZX}(t) = \sigma^0_{ZX} H(t); \tag{78}$$

where σ^0_{ZX} is a constant and H(t) is the Heaviside step function. Two types of boundary conditions were considered for the back face: fixed and free. Because the analytical solution for this problem is available, the behavior of the element can be compared with the analytical predictions to establish its accuracy.

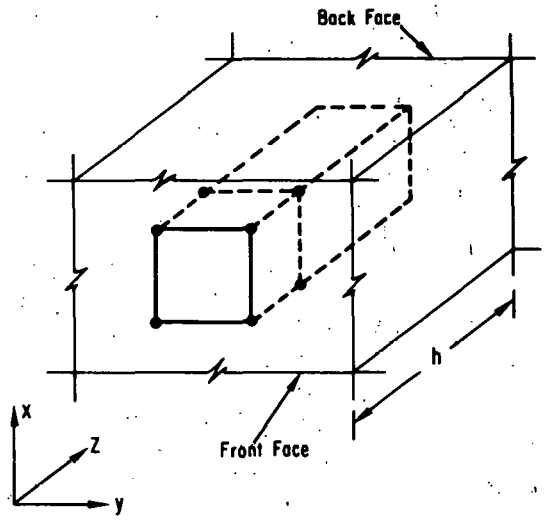

Fig. 19. "Bar" Model for Studying Plane-wave Propagation in an Infinite Plate

A finite-element mesh (see Fig. 19) consisting of 50 solid hexahedral elements was used to represent a "bar-type" model through the plate thickness; the cross-sectional area of the bar was 1 cm^2. The analytical solution to this problem consisted of motion only in the X direction. Therefore, our nodal fixities were such that only nodal motion in the X direction was permitted. The shear stress σ^0_{ZX} in Eq. 78 was set equal to 10 MPa. The plate density ρ and shear modulus G were taken to be 7.8 g/cm^3 and 80 GPa, respectively.

The analytical solution to this problem is a plane shear wave (S wave) of stress magnitude σ^0_{ZX} traveling in the Z direction with a wave speed C_S given by

$$C_S = \sqrt{\frac{G}{\rho}}. \tag{79}$$

Once the wave front passes through a section, the particles in the stressed zone attain a velocity in the X direction $v_X^{(P)}$ given by

$$V_X^{(P)} = \frac{\sigma^0_{ZX}}{\sqrt{\rho G}}. \tag{80}$$

The analytical-numerical comparisons for this problem are shown in Figs. 20-23. The numerical results for the case in which the back face is

free compare well with the analytical solution. In Fig. 20 the particle velocities are plotted for points that are in a zone 24 cm from the loaded face. The agreement of wave-arrival times and particle velocities is very good. The initial plateau is due to the incident S wave, and the second is due to the reflected S wave. The doubling in velocity upon passage of the reflected wave agrees with the analytical results. In Fig. 21, numerical results for the stress-time history at the plate midthickness are compared to the analytical solution. Here also the wave-arrival times and stress magnitudes are in good agreement with the analytical solution. The incident S wave is seen to increase the stress state in the element from zero to the applied stress (10 MPa), while the reflected wave reduces the stress state back to zero.

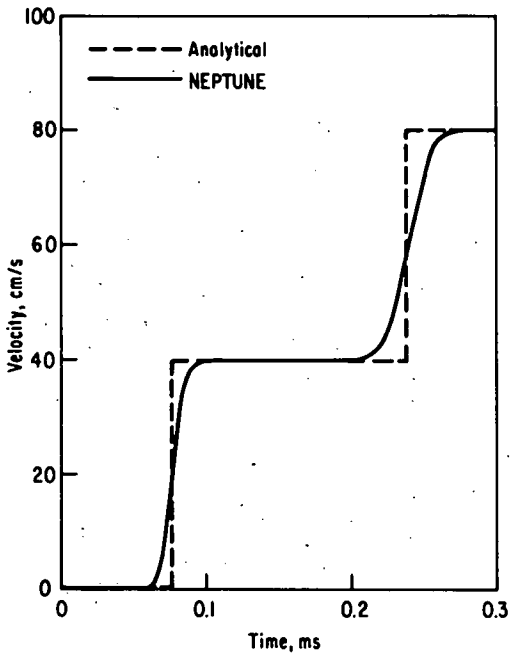

Fig. 20

Particle Velocity in a Zone 24 cm from the Loaded Face: Free Back Face. Calculations were performed using artificial viscosity.

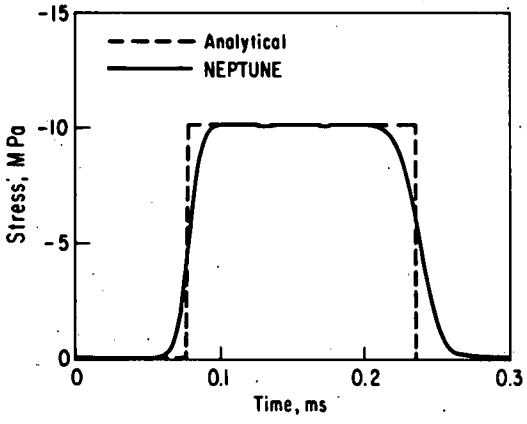

Fig. 21

Stress–Time History at Plate Midthickness: Free Back Face. Calculations were performed using artificial viscosity.

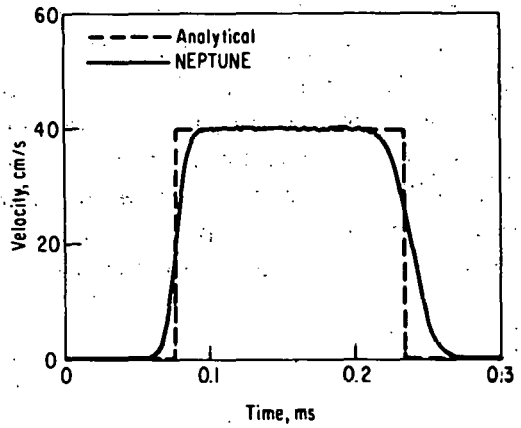

Fig. 22. Particle Velocity at a Zone 24 cm from the Loaded Face: Fixed Back Face. Calculations were performed using artificial viscosity.

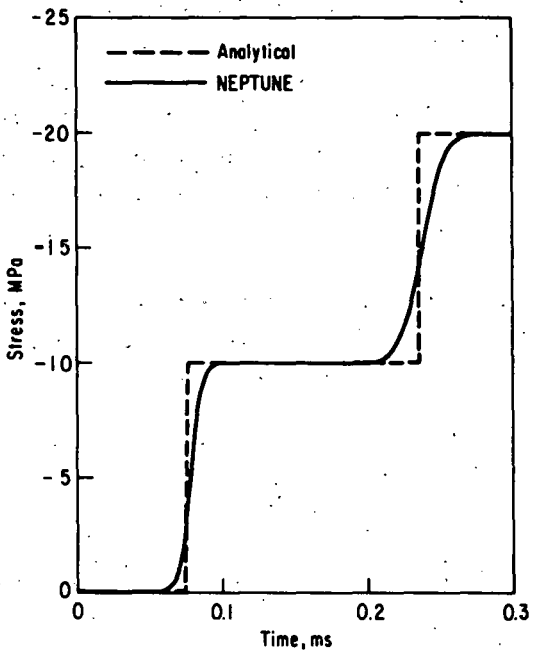

Fig. 23. Stress-Time History at Plate Mid-thickness: Fixed Back Face. Calculations were performed using artificial viscosity.

The particle velocity and stress-time history for the case in which the back face is fixed are shown in Figs. 22 and 23, respectively. The difference in response between the free- and fixed-face cases is in the behavior after the reflected wave passes through the element. For the free-faced case the reflected wave doubles the particle velocity and reduces the stress state back to zero. In contrast, when the back face is fixed, the reflected wave reduces the particle velocity back to zero and doubles the stress. These results agree with elementary wave-propagation theory and indicate that the newly developed three-dimensional solid element is representing this behavior accurately.

G. Dynamic Response of Large Pool-type Deck Structures to an HCDA

Figure 24 is a schematic elevation view of a 1200-MWe pool-type reference system. The reactor-core region was designed to provide 3000 MW of thermal power with sodium entering at about 371°C (700°F) and leaving at about 538°C (1000°F). The main components of the pool-type LMFBR system are shown: the reactor-core region, internal heat exchangers (IHX's), primary pumps, the core-support structure, primary and secondary tanks, and the shield-deck structure. The instrument tree and fuel-handling machinery are not shown. Figure 25 shows the plan view of the reference reactor. The primary vessel contains three primary pumps, six IHX's, and two storage baskets. The basic dimensions of the pool reactor used in this preliminary study are shown in Fig. 26.

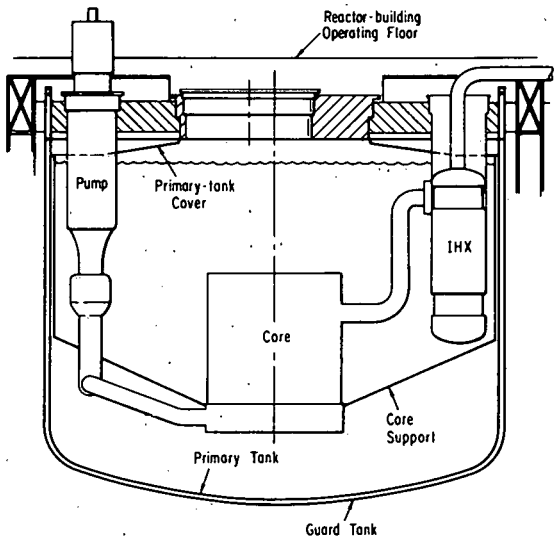

Fig. 24. Schematic Elevation View of Pool-type Reactor Based on Cold-pool (EBR-II) Design

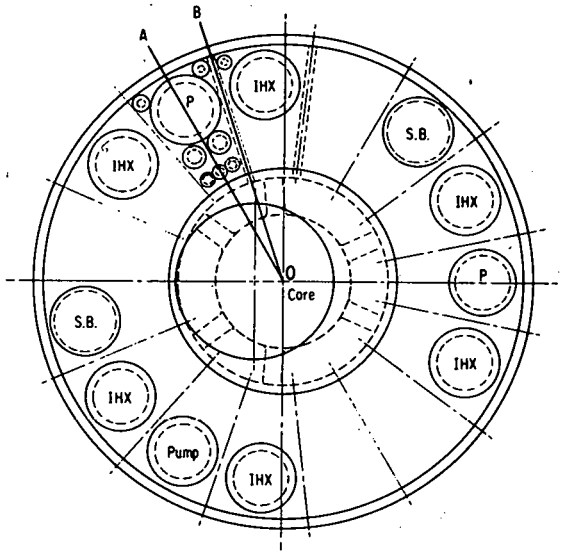

Fig. 25. Schematic Plan View of Pool-type Reactor (1200 MWe)

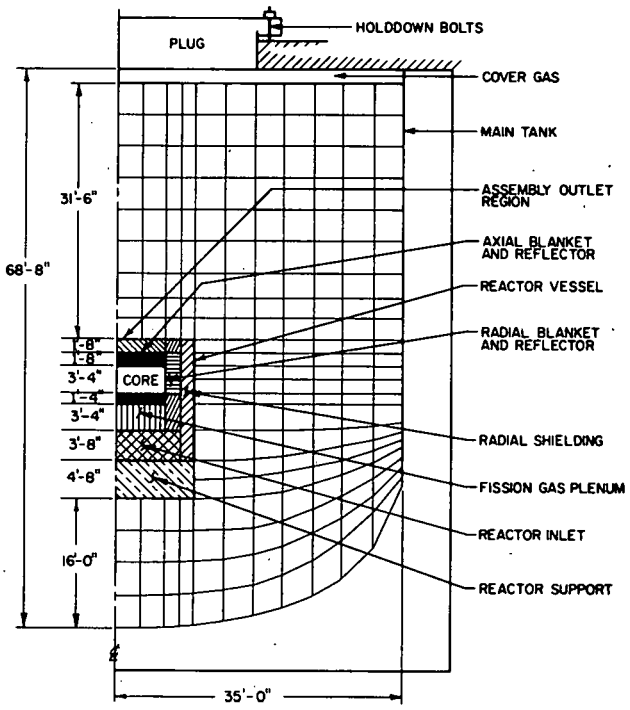

Fig. 26

Model Used in REXCO-HEP Calculations. Conversion factors: 1 ft = 0.305 m, 1 in. = 2.54 cm.

The shield deck itself is an annular structure supported by steel columns embedded in the surrounding concrete radial biological shield. The major structural components of the deck are the radial I-beams, the bottom annular plate, and the inner ring that supports the rotating plugs. The radial beams form a "spoked" type of structure with the central inner ring as the hub. The deck is, in general, a concrete-filled, beam-plate composite

structure which provides, in most designs, support for the pumps and heat exchangers, primary and guard tanks, and sufficient radiation shielding.

Pressure loadings (Fig. 27) used in this study were obtained from output of the REXCO-HEP[10] containment code. It must be pointed out that the "zero" time shown in Fig. 27 is referred to the beginning of slug impact. Relative to the beginning of the accident, slug impact occurs at about 95 ms. The peak pressure was 10.4 MPa (104 MD/cm^2) and occurred at 9.7 ms. The pressure decreases in an oscillatory manner to a quasi-equilibrium pressure at the end of the calculations. Using the above code, a finite-element model was designed to assess the ability of a pool-type LMFBR shield deck to sustain an energetic HCDA.

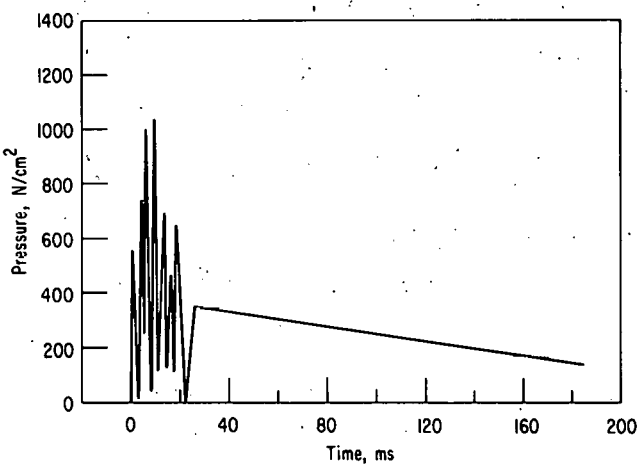

Fig. 27. Pressure Loading on Deck Structure

From the plan view of a conceptual representation of an expanded EBR-II-type deck, it was determined that there is a reasonable amount of symmetry in the structure, and that an initial model would consist of a 12° sector encompassing one radial I-beam and one-half of a typical in-tank component (e.g., intermediate heat exchanger, pump, or storage basket). The model is shown in Fig. 28. The structural components modeled are the main radial I-beam, the component-support I-beam, the inner ring, the concrete fill, and the in-tank component nozzles. Although the rotating plug is not modeled explicitly, its mass was taken into account by distributing it along the inner ring. Similarly, the pressure load acting on the plug assembly was treated as a vertical-force line load acting on the inner ring of the deck.

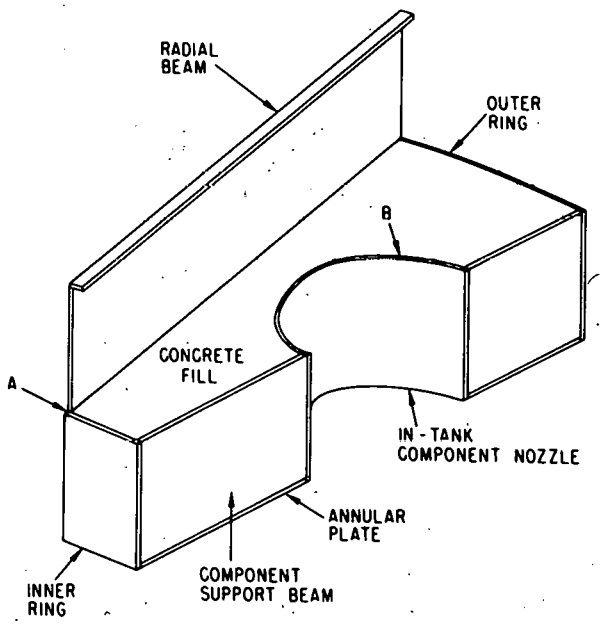

Fig. 28. Sector Model for Pool-type Deck Structure

Two separate models were generated for this study. The first model accounts for the mass of the concrete, but ignores its structural effect. The concrete mass is distributed along the beams, while the mass of a typical in-tank component is taken into account as concentrated masses located along the nozzle. The second model, which is similar, accounts for the structural effect of the concrete fill as well as its mass.

The finite-element discretization of our models is shown in Figs. 29-32. Figure 29 shows the discretization of the entire model; Figs. 30-32 illustrate the discretization of the various deck components. The material properties used for the various structural members and the concrete biological shielding are listed in Table III. The steel was assumed to follow a bilinear, universal stress-strain curve based upon the mechanical properties listed in Table III.

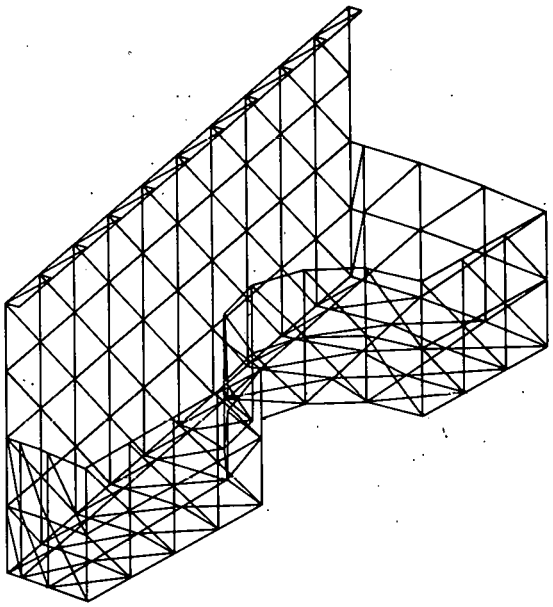

Fig. 29. Complete Structure Plot of Finite-element Model for Deck Structure of a 1200-MWe Reference Reactor

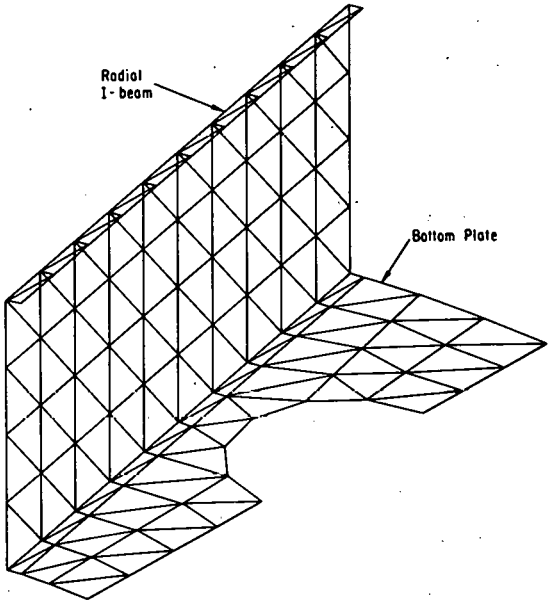

Fig. 30. Multiple-component Plot of Radial I-beam and Bottom Annular Plate of the Deck

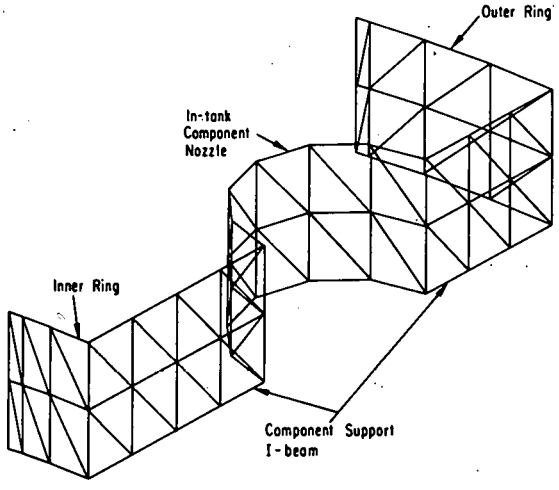

Fig. 31. Multiple-component Plot of Inner Ring, Component-support I-beam, Component Nozzle, and Outer Ring

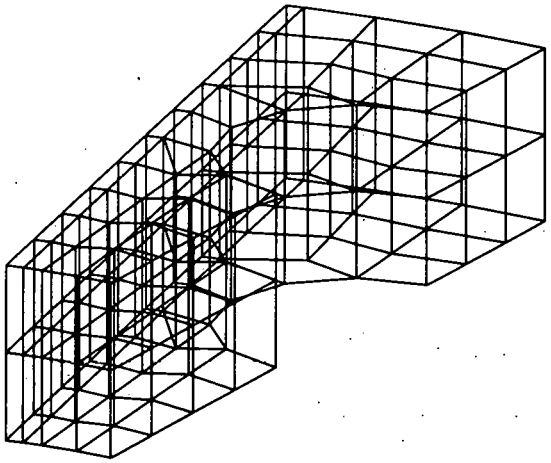

Fig. 32. Discretization of Concrete Fill

TABLE III. Material Properties for Components of the Deck Structure

	T1 Steel	Concrete
Young's modulus (GPa)	206	31.7
Poisson's ratio	0.30	0.18
Yield stress (MPa)	620	-
Ultimate stress (MPa)	724	-
Tangent modulus (MPa)	620	-

The above models were loaded according to the pressure-time curve shown in Fig. 27. This pressure was applied uniformly to the underside of the annular plate. As mentioned above, the plug load was considered to be a line load acting on the inner ring. It was assumed that the in-tank component did not contribute to the loading, except for its mass effect.

The boundary conditions applied to this deck structure are obtained from the following basis. At the outer periphery the deck is supported by vertical columns which connect directly to the beams. The beams and columns are considered to be connected by a welded, stiffened corner, which corresponds to a "fixed-end" boundary condition.

At the deck's inner periphery the choice of the boundary condition is not as obvious. Here the boundary condition is determined by the manner in which the rotating-plug assembly is connected to the deck. The rotating-plug assembly would be connected to the top area of the inner ring with a substantial holddown bolting system. Because of this holddown system and the large stiffness of the plug assembly, there was believed to be little radial differential movement between the plug assembly and the deck at the top of the inner ring. Therefore, the top of the inner ring was assumed to move vertically and to be restricted from radial motion. This boundary condition corresponds to a "pinned-end" condition in which vertical motion is permitted. The remainder of the inner ring is separated from the plug assembly by a relatively small clearance gap. Depending on the size of this gap, the plug assembly may further restrict the inner ring from rotating during loading. This motion constraint would occur when the gap dimension is small. In contrast, if the gap is relatively large, no restraint would occur. For this study we consider only the case of a small gap and, therefore, restrain the inner ring from rotations. Thus, for this condition the movement of the entire inner ring is restricted to vertical motion.

The vertical displacement of the radial I-beam at its connection to the inner ring is shown in Fig. 33 for both models. It is seen that the structural effect of the concrete fill was to reduce by 31% the peak displacement of the deck from 5.2 to 3.6 cm. The peak displacements occurred at 30.8 ms for the model that neglected the structural effect of concrete and at 21 ms for the model that included the structural strength.

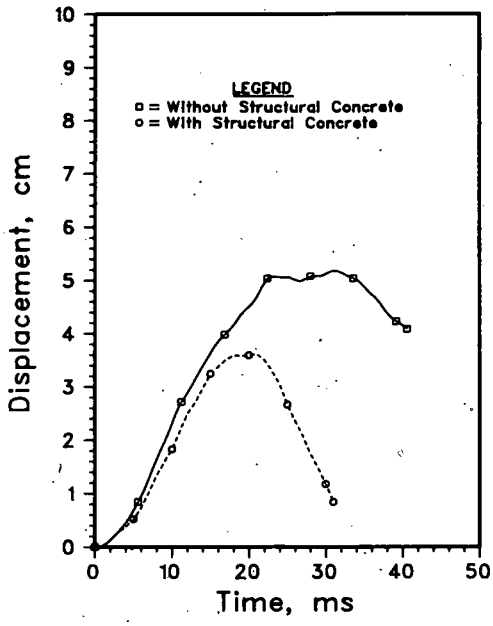

Fig. 33

Vertical-displacement Histories of Radial I-beam at Its Connection to Inner Ring with and without the Structural Effect of Concrete

The above short study illustrates the use of the continuum element for treating the structural effect of a deck's concrete fill. A more detailed study on deck response will be conducted at a later date to ascertain the effect of various design parameters.

H. Fluid-Structure Interaction of a Pool Reactor In-tank Component due to Pressure-wave Propagation

In the design of a pool-type reactor (Figs. 24 and 25) several vital components such as the primary pumps and the intermediate heat exchangers are contained within the primary tank. Typically, these components are suspended from the deck structure and largely submersed in the sodium pool. Because of this positioning, these components are vulnerable to structural damage due to pressure-wave propagation arising in the tank from an HCDA. To assess the structural integrity of these components, we must perform a three-dimensional dynamic analysis which accounts for the fluid-structure coupling.

The loading for this problem is from a short-duration energy source which creates pressure waves that propagate through the sodium pool and load the embedded component, the surrounding primary tank, and the deck structure.

For a preliminary study of this complex problem, we developed a simple model which has many of the salient features of this fluid-structural component system. To begin, we modeled the primary tank and the in-tank component as deformable elastoplastic structures made of Type 304 stainless steel, the sodium pool as an inviscid, compressible fluid, and the deck to be rigid and fixed in space. The effects of slug impact are not addressed. Subsequent models will include both a deformable deck and slug-impact effects.

A reasonable model can be developed by assuming a 12° repeated symmetry of the system. Therefore a model (Fig. 34) that includes a 12° sector of the sodium pool, one-half of an in-tank component (primary pump or intermediate heat exchanger), and a 12° sector of the primary tank is sufficient. Because of these symmetries, we can define the symmetry planes shown in Fig. 34. Symmetry plane S1 is the plane OACEO, which originates along the axial centerline of the tank and passes through the axial centerline of the in-tank component. The symmetry plane S2 OBDEO also originates along the tank's axial centerline, but it passes halfway between adjacent in-tank components. The final symmetry plane S3 ECDE is a horizontal plane.

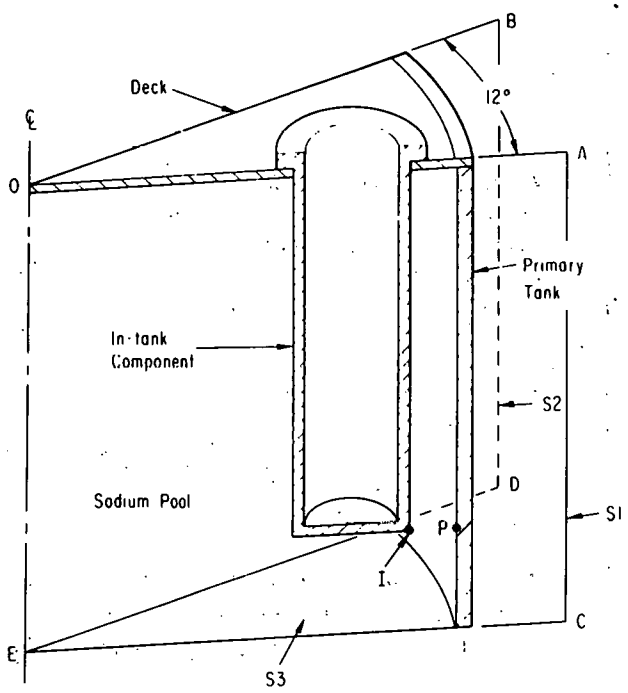

Fig. 34. Simple Model of In-tank Component, Primary Tank, Sodium Pool, and Deck

The finite-element mesh for our model is shown in Figs. 35-37. The entire mesh (Fig. 35) consists of 80 triangular plate/shell elements and 127 hydrodynamic elements. A clearer picture of the components of our mesh is shown in the substructure plot, which is a plot of an individual component or a group of components.

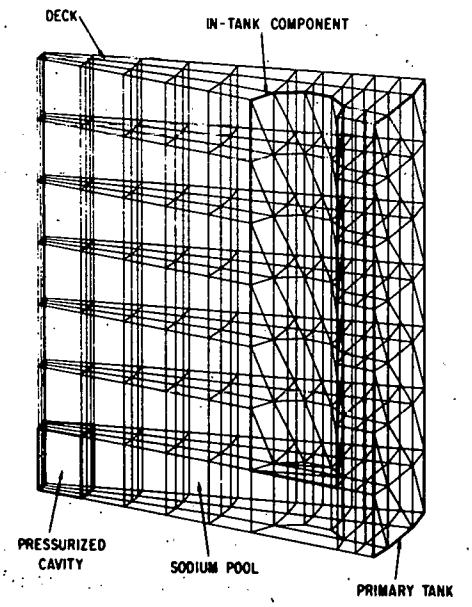

Fig. 35. Finite-element Mesh of Simple Model Showing In-tank Component, Primary Tank, Pressurized Cavity, Sodium Pool, and Deck

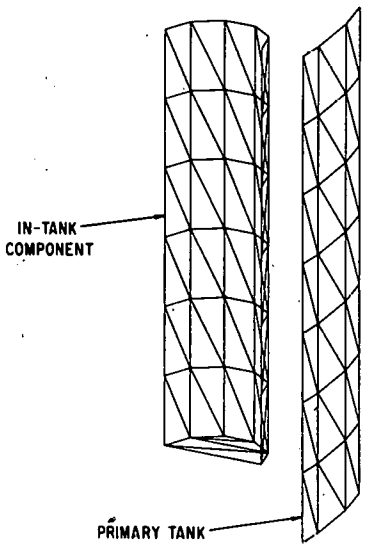

Fig. 36. Finite-element Mesh of Primary Tank and In-tank Component

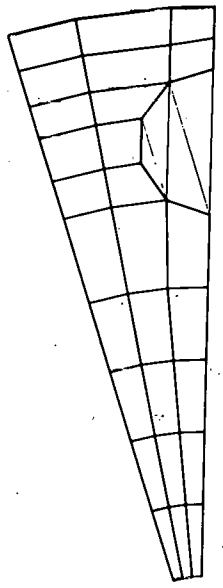

Fig. 37. Plan View of Finite-element Mesh for Simple Model

Figure 36 is a plot of only the structural components of the model: the in-tank component and the primary tank. Our model for the in-tank component consists of 38 triangular plate elements, which simulate the entire length but only one-half of the circumference of an in-tank component. The boundary conditions at the top are zero displacements and rotations. The nodes that lie in the symmetry plane S1 are confined to motion only in that plane. The remaining nodes of the component model are free to move arbitrarily in three-dimensional space.

The model for the primary tank consists of 42 plate elements. The boundary conditions at the top of the tank are zero displacement and rotations that simulate the tank's attachment to the rigid deck. In contrast, the boundary conditions at the bottom of the tank model are such that these nodes are allowed to translate in the symmetry plane S3. Rotations that preserve the symmetry are allowed.

The nodes that are connected entirely by fluid elements are free to move arbitrarily in three-dimensional space, except for those that are restricted to motion in a symmetry plane. Figure 37 is a plane view of our model.

For our preliminary study, the pressure volume curve (Fig. 38) described by Amorosi et al.[2] is used to describe the expansion of the core region during an HCDA. The resulting displacement history for the in-tank component was obtained. The radial displacement-time history of the bottom of the in-tank component, given in Fig. 39, shows a maximum displacement of 30.7 cm at 50 ms after the initiation of cavity pressurization. At this time the clearance between the in-tank component and the primary tank is 94 cm.

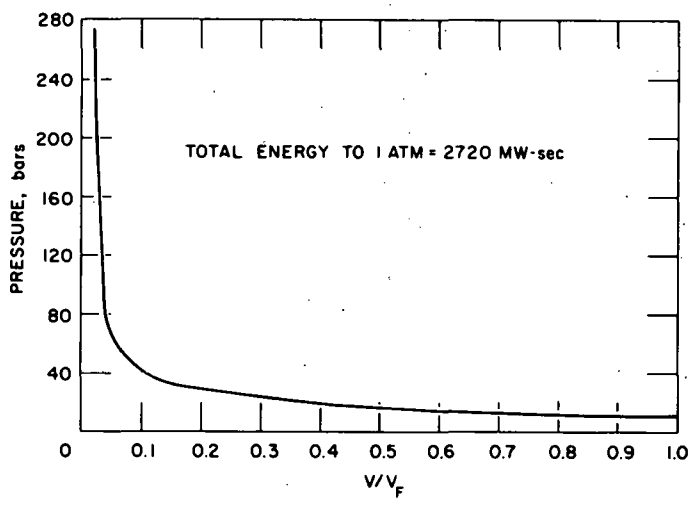

Fig. 38

Pressure-Volume Curve of Core Expansion

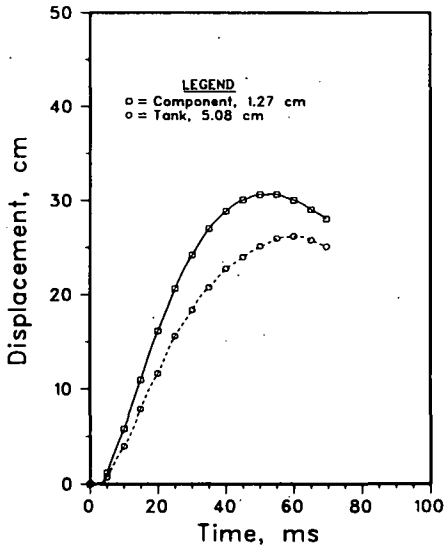

Fig. 39

Radial-displacement Histories of Bottom of In-tank Component and Primary Tank: Points I and P, Respectively, of Fig. 34

This preliminary study showed that the dynamic response of an in-tank component is such that the peak displacement of the component is sufficiently small so that contact between the component and the tank is not anticipated.

ACKNOWLEDGMENTS

We thank the following people for their help and support during this work: Dr. T. B. Belytschko for his helpful suggestions during the development of the hexahedral element, Dr. H. L. Schreyer for the stimulating discussions during the development of the constitutive algorithm, and Drs. S. H. Fistedis and J. M. Kennedy for their interest and support of this program. This work was performed in the Computational Mechanics Section of the Engineering Mechanics Program of the Reactor Analysis and Safety Division, Argonne National Laboratory.

REFERENCES

1. A. H. Marchertas and T. B. Belytschko, *Nonlinear Finite-element Formulation for Transient Analysis of Three-dimensional Thin Structures,* ANL-8104 (June 1974).
2. A. Amorosi, E. Hutter, T. J. Marciniak, H. O. Monson, R. W. Seidensticker, and W. R. Simmons, *An Overview of Pool-type LMFBRs: General Characteristics,* ANL-76-61 (May 1976).
3. Primary Systems Study Group, ANL, personal communication.
4. O. C. Zienkiewicz, *The Finite Element Method in Engineering Science,* McGraw-Hill Book Co., Inc., London (1972).
5. J. M. Kennedy and T. B. Belytschko, *Energy Source and Fluid Representation in a Structural Response Code--STRAW,* ANL-8140 (May 1975).
6. R. D. Krieg and S. W. Key, "Transient Shell Response by Numerical Time Integration," *2nd U. S. Japan Seminar on Matrix Methods in Structural Analysis,* Berkeley, Calif. (1972).
7. J. Barlow, *Optimal Stress Locations in Finite Element Models,* Int. J. Num. Meth. Eng. *10,* 243-251 (1976).
8. T. Belytschko, R. L. Chiapetta, and H. Bartell, *Efficient Large Scale Nonlinear Transient Analysis by Finite Elements,* Int. J. Num. Meth. Eng. *10,* 579-596 (1976).
9. T. Belytschko, *WHAM--Waves in Hysteretic Arbitrary Media and Structures,* University of Illinois at Chicago Circle (1974).
10. Y. W. Chang and J. Gvildys, *REXCO-HEP: A Two-dimensional Computer Code for Calculating the Primary System Response in Fast Reactors,* ANL-75-19 (June 1975).

Distribution for ANL-80-26

Internal:

W. E. Massey
J. A. Kyger
R. Avery
L. Burris
D. W. Cissel
S. A. Davis
B. R. T. Frost
E. V. Krivanec
R. J. Teunis
C. E. Till
R. S. Zeno
L. W. Deitrich
J. F. Marchaterre
A. J. Goldman
D. Rose
R. H. Sevy
I. Bornstein
W. C. Lipinski
J. B. Heineman
D. H. Lennox
J. H. Tessier
D. R. Pedersen
C. E. Miller
T. C. Chawla
D. H. Cho
C. E. Dickerman
F. E. Dunn
A. DeVolpi
M. Epstein
S. H. Fistedis
A. E. Klickman
J. M. Kramer
P. A. Lottes
R. A. Noland
A. B. Rothman
B. W. Spencer
D. P. Weber
H. U. Wider
Y. W. Chang
C. Fiala (10)
J. Gvildys
J. M. Kennedy
R. F. Kulak (10)
A. H. Marchertas
M. T. Abdel-Moneim
H. J. Petroski
R. W. Seidensticker
H. Schreyer
C. Y. Wang
W. Zeuch
D. Myers (5)
G. Ridges
A. B. Krisciunas
ANL Contract File
ANL Libraries (5)
TIS Files (6)

External:

DOE-TIC, for distribution per UC-79p (197)
Manager, Chicago Operations and Regional Office, DOE
Chief, Office of Patent Counsel, DOE-CORO
Director, Technology Management, DOE-CORO
Director, DOE-RRT (2)
President, Argonne Universities Association
Reactor Analysis and Safety Division Review Committee:
S. Baron, Burns and Roe, Inc.
J. R. Dietrich, Combustion Engineering, Inc.
W. Kerr, U. Michigan
M. Levenson, Electric Power Research Inst.
S. Levy, S. Levy, Inc.
D. Okrent, U. California, Los Angeles
N. C. Rasmussen, Massachusetts Inst. Technology